

Ab initio study on influence of dopants on crystalline and amorphous Ge₂Sb₂Te₅

Eunae Cho,¹ Seungwu Han,^{1,a)} Dohyung Kim,² Hideki Horii,² and Ho-Seok Nam³

¹Department of Materials Science and Engineering, Seoul National University, Seoul 151-744, Korea

²Process Development Team, Memory R&D Center, Semiconductor Business, Samsung Electronics, Yongin 446-71, Korea

³Center for Materials and Processes of Self-Assembly and School of Advanced Materials Engineering, Kookmin University, Seoul 136-702, Korea

(Received 10 November 2010; accepted 6 January 2011; published online 28 February 2011)

The pronounced effects of dopants such as Si, N, and O atoms, on material properties of Ge₂Sb₂Te₅ are investigated at the atomic level using *ab initio* calculations. In the crystalline phase, stable doping sites are determined by characteristic chemical bonds such as Ge–N and Ge–O. The comparison of lattice parameters between theory and experiment supports the existence of dopants at vacant or interstitial positions. The electronic density of states indicate that the localization at the valence top increases with N- or O-doping, explaining the increase of resistivity in experiments. The amorphous structures of doped Ge₂Sb₂Te₅ are obtained by melt-quench simulations and they are well understood by selective bonds between dopants and host atoms. The chemical bonds around dopants are more favorable in the amorphous phase than in the crystalline state, accounting for increased amorphous stability of doped Ge₂Sb₂Te₅. The atomic and electronic structures of amorphous Ge₂Sb₂Te₅ do not support a viewpoint that the bonding nature is changed toward the covalent character upon doping. The recrystallization of doped Ge₂Sb₂Te₅ is also simulated and it is directly confirmed that the crystallization process of doped Ge₂Sb₂Te₅ is slowed down by dopants. © 2011 American Institute of Physics. [doi:10.1063/1.3553851]

I. INTRODUCTION

Ge₂Sb₂Te₅ (GST) is a representative phase-changing chalcogenide compound that shows stable and fast phase transitions between crystalline and amorphous phases. GST has been actively employed in optical disks such as DVD, and more recently it is applied to solid state memories such as the phase-change random access memory (PRAM).¹ Even though undoped GST is already superior to other material families in many respects, various efforts have been devoted to tailoring physical properties of GST with an aim to enhance the device performance further. Among them, a popular approach is to incorporate small amounts of dopants such as Si,^{2–4} N,^{4–13} and O atoms.^{10,14} The purpose of doping slightly varies with application targets; when applied to optical memories, it was noted that N-doped GST improves the stability of amorphous marks, as evidenced by the increased crystallization time.^{6,8} In PRAM, N-doping provides a convenient solution to reduce the electric current required to transform the crystalline GST into the amorphous phase (so called reset currents).⁹ This is because N doping increases resistivity in the crystalline phase. Similar benefits were also achieved with Si (Ref. 3) and O (Refs. 10, 14) dopants.

The pronounced effects of dopants have been explained considering two factors. First, it has been observed that the dopants tend to reduce the grain size,^{4,7,8,15} possibly caused by dopant segregation near grain boundaries in the form of nitrides or oxides.^{4,6,16} The resistance of the crystalline phase

would increase due to additional electron scattering from grain boundaries.⁹ As a more intrinsic origin, it was also suggested that the dopants affect the bonding character to be more covalent or induce lattice strain as they take up tetrahedral sites.¹⁰ However, these assumptions have not been fully supported by microscopic evidence and the fundamental understanding on the role of dopants is still elusive, limiting efforts to identify optimal dopant species and concentrations.

Theoretically, *ab initio* molecular dynamics (MD) simulations have provided rich information on amorphous structures of undoped GST.^{17–25} It has been consistently demonstrated that the local order is different between crystalline and amorphous GST (a-GST), which accounts for the distinct physical properties between the two phases.^{19,24,26} In contrast, there are few studies on doped GST.^{16,27,28} In Refs. 16 and 27, N atoms in a-GST were found to dominantly bond with Ge atoms. The N dopants in the hexagonal phase were studied in Ref. 28 and it was found that the N₂ molecule was more stable than interstitial N atoms. However, to gain further insights into the influence of dopants on the crystalline and amorphous GST, a more systematic study considering both phases is strongly required. Furthermore, various types of dopants need to be compared simultaneously to map out the relationship between the chemical nature of dopants and the change in atomic and electronic structures, thereby providing guideline to select optimal dopants. Motivated by this situation, we carry out in this work extensive *ab initio* calculations to reveal atomic and electronic structures of GST doped with Si, N, and O atoms, which are currently under active investigations. In the present work, we focus on atomically resolved dopants in the crystalline and amorphous GST but it is noted that extrinsic effects

^{a)}Author to whom correspondence should be addressed. Electronic mail: hansw@snu.ac.kr.

such as segregation of dopants near grain boundaries may also play significant roles in real samples.

II. COMPUTATIONAL METHODS

We perform *ab initio* calculations based on the density functional theory. The Vienna *Ab-initio* Simulation Package²⁹ is used for molecular dynamics simulations and the electronic structure calculations. The projector-augmented-wave pseudopotentials³⁰ are used to describe electron-ion interactions. For the exchange-correlation energies between electrons, the generalized gradient approximation based on the Perdew–Burke–Ernzerhof (PBE) functional³¹ is employed. The energy cutoff for the plane-wave basis expansion is chosen to be 131, 184, 210, and 220 eV for MD simulations of undoped, Si-, N-, and O-doped GST, respectively. The higher energy cutoff of 250 eV is used when the structural relaxation is performed. The atomic positions are relaxed until the Hellmann–Feynman force on each atom is reduced to within 0.03 eV/Å.

The k points in the first Brillouin zone are sampled differently according to the supercell size and computational mode. In studying dopants in crystalline GST including 72 atoms within the supercell (Sec. III), a $2 \times 2 \times 2$ regular mesh is used consistently. When a larger size of 216-atom supercell is used for studying amorphous phase (Secs. IV A and IV B), the Γ point is sampled for MD simulations and the ensuing structural relaxation is performed with the single (0.25, 0.25, 0.25) point. In plotting the density of states (DOS), a $2 \times 2 \times 2$ regular mesh is used. Finally, the single (0.25, 0.25, 0.25) point is used in the recrystallization simulation on the 72-atom supercell (Sec. IV C).

III. DOPANTS IN CRYSTALLINE $\text{Ge}_2\text{Sb}_2\text{Te}_5$

A. Stable doping sites

First, we discuss on stable sites of dopants in crystalline (cubic) GST (c-GST). Figure 1(a) shows five representative doping types, X_{Ge} , X_{Sb} , X_{Te} , X_{vac} , and X_i , where X indicates one of Si, N, and O atoms. X_{Ge} , X_{Sb} , and X_{Te} mean the substitutional doping in which the dopant X replaces Ge, Sb and Te atoms, respectively. For X_{vac} , the dopant is placed on an empty lattice site of c-GST. Finally, a dopant at the interstice inside the lattice cube is denoted as X_i . Initially, a dopant at X_i is placed at the lattice-cube center corresponding to the tetrahedral site, but they relax away from this position significantly (see below). As the cation sublattice sites (or A sites) are randomly occupied with Ge, Sb, and vacancies, local configurations are not unique for a given doping type. To account for the configurational variation, we randomly select five sites for each doping type and average the results.

We use a $13.7 \times 13.7 \times 12.2 \text{ \AA}^3$ supercell comprising 72 atoms and introduce one dopant atom per supercell. This corresponds to a doping concentration of 1.4 at. %. To compare the relative stability among dopant sites, we calculate the formation energy (E_{for}) as follows:

$$E_{\text{for}} = E_{\text{tot}}(X\text{-doped } c\text{-GST}) - E_{\text{tot}}(\text{undoped } c\text{-GST}) - \mu_X + \mu_0, \quad (1)$$

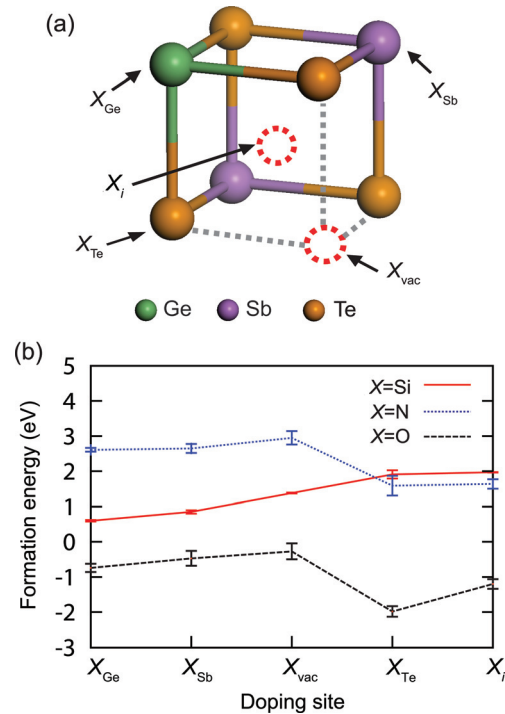


FIG. 1. (Color online) (a) Five representative doping sites in the crystalline $\text{Ge}_2\text{Sb}_2\text{Te}_5$. (b) The formation energy with respect to the dopant species and doping sites.

where E_{tot} is the total energy per supercell with or without dopants, and μ_X is the chemical potential of the dopant X . The last term in Eq. (1), μ_0 , indicates the chemical potential of Ge, Sb, and Te for X_{Ge} , X_{Sb} , and X_{Te} , respectively, while it is zero for X_{vac} and X_i . The chemical potentials for Si, Ge, Sb, and Te atoms are set to their total energies in the most stable crystalline structure. For N and O, half of the total energy of the diatomic molecule is used as the chemical potential.

Figure 1(b) displays the computed E_{for} 's averaged over five configurations. The standard deviations are denoted by error bars. The small dopants such as N and O show wider error bars than Si dopants. This is because N and O form bonds with mainly Ge or Sb atoms, and therefore more sensitive to A -site variations. For Si, the most stable site is found to be Si_{Ge} . This is because Si atoms are chemically most similar to Ge atoms. As such, Si_{Ge} gives rise to little lattice deformations around the dopant site.

In Fig. 1(b), E_{for} 's for N and O dopants differ by 3–4 eV even though the two elements are next to each other in the Periodic Table. The dissociation energies of N_2 and O_2 molecules are calculated to be 9.53 and 5.61 eV within the present computational conditions, respectively. [Experimental values are 9.79 eV (N_2) and 5.15 eV (O_2).³²] Therefore, the large, positive E_{for} 's for N dopants mainly originate from the strong binding energy of N_2 molecules. This also excludes a possibility that N atoms are doped through spontaneous dissociation of N_2 molecules. This result is consistent with other calculations on N-doped hexagonal GST (Refs. 4 and 28) and also experimental observations of N_2 molecules in N-doped GST.³³ However, ion collisions during the reactive sputtering

method, the most favored process to grow doped GST, may generate atomic nitrogen from N_2 molecules which is then incorporated into the thin film. Furthermore, the similarities between samples doped by reactive sputtering and ion implantation¹⁰ also supports that the atomically resolved nitrogen as studied in this work may actually be present in significant amounts and affect various properties of doped GST.

Figure 1(b) shows that N and O atoms favor X_{Te} or X_i over A -site doping. The N atoms in Te sites move along the diagonal direction and form three bonds with Ge or Sb atoms. A typical geometry is presented in Fig. 2(a) which shows that the N dopant is bonded with three Ge atoms. It is found that E_{for} 's among the five statistical samples are decreased with the increasing number of Ge-N bonds. This suggests that Ge-N bonds are more stable than Sb-N bonds. A similar observation is also found for O_{Te} ; O dopants shift away from the original position and form bonds with neighboring Ge atoms. [See Fig. 2(b).] In contrast to predominant threefold coordination of N_{Te} , most O_{Te} dopants are bivalent. On the other hand, N_i and O_i dopants typically relax toward a cube corner (initially they were placed at the tetrahedral site) and push out nearby Te atoms, thereby establishing bonds with Ge or Sb atoms [see Figs. 2(c) and 2(d)]. As a result, the local configurations are similar to those of X_{Te} except for extra N-Te or O-Te bonds. The large displacement of Te atoms is facilitated by the nearby A -site vacancy.

The preferential Ge-N and Ge-O bonds can be understood based on Pauling's electronegativities which are 3.04 (N), 3.44 (O), 2.01 (Ge), 2.05 (Sb), and 2.1 (Te). Therefore, the largest difference in electronegativity results when N and O dopants establish chemical bonding with Ge atoms. The stable Ge-N and Ge-O bonds can also be inferred by the existence of crystalline phases of Ge_3N_4 and GeO_2 ; for germanium nitrides, the most stable phase is β - Ge_3N_4 with Ge atoms in the tetrahedral configuration and N atoms in a

planar, threefold coordination. The average Ge-N bond length in β - Ge_3N_4 is 1.85 Å from the present calculation. On the other hand, there are two phases of germania with similar energies: β -quartz and rutile structures. The two phases differ in energy by only 0.01 eV per formula unit within the present calculation. However, the local configurations are different as (Ge, O) show (4, 2) and (6, 3) coordinations in β -quartz and rutile structures, respectively. This also results in distinct Ge-O bond lengths of 1.78 (β -quartz) and 1.89 (rutile) Å.

The local structures in Fig. 2 resemble the crystalline structures of Ge_3N_4 and GeO_2 , accounting for the stability of X_{Te} and X_i . Consistently, the average Ge- X_{Te} or Ge- X_i bond lengths [2.05 (N_{Te}), 1.98 (O_{Te}), 1.93 (N_i), 1.94 (O_i) Å] are close to the above theoretical bond lengths in crystalline phases albeit slightly longer. Since these bond lengths are much shorter than the average nearest-neighbor distance in c-GST (~ 3 Å), Ge-N and Ge-O bonds give rise to significant lattice deformations as visible in Fig. 2. We also note that the local structure is more favorable for O_{Te} than N_{Te} ; in β -quartz GeO_2 , the O atom is twofold coordinated with the Ge-O-Ge angle of 130° . This configuration is closely reproduced by O_{Te} in Fig. 2(d). By contrast, N atoms in β - Ge_3N_4 form a planar bonding with three Ge atoms but the local configuration around N_{Te} in Fig. 2(a) is rather distorted from this geometry due to the orthogonal p -bonding network in c-GST. This may contribute in part to the large difference in E_{for} between N_{Te} and O_{Te} .

B. Influence of dopants on lattice parameters

The lattice distortion induced by dopants affects lattice parameters. In order to analyze this quantitatively, we examine crystal structures at high doping concentrations. In Fig. 3, variations in lattice parameters are computed when 4 or 8 dopants are introduced in each 72-atom supercell with a certain doping type, which corresponds to concentrations of ~ 5 or ~ 10 at. %, respectively. Both cell shapes and volumes are optimized in addition to the atomic relaxation. To facilitate the comparison with experiment, the equilibrium lattice parameter is set to $(V_{relaxed}/10)^{1/3}$ with $V_{relaxed}$ being the final volume after cell optimization. The lattice parameter for undoped c-GST is 6.1 Å, in good agreement with the experimental value of 5.99 Å.

In spite of chemical diversity between studied dopants, lattice parameters in Fig. 3 show systematic behaviors common to all dopants. First, all interstitial dopants increase the lattice parameters, which is certainly a result of positive strain induced by dopants. The expansion is most pronounced for Si_i due to the large atomic size. In contrast, the most stable Si_{Ge} dopants reduce the lattice parameter because the atomic size of Si is smaller than for Ge. In Ref. 15, the lattice parameters of Si-doped c-GST were measured with respect to the dopant concentration and they are indicated by empty circles in Fig. 3(a). This expansion is not explained by Si_{Ge} dopants and may indicate the presence of some amounts of Si_{vac} or Si_i . [From the energetic point of view, Si_{vac} would be more favorable as shown in Fig. 1(b).] On the other hand, the experimental lattice parameters for

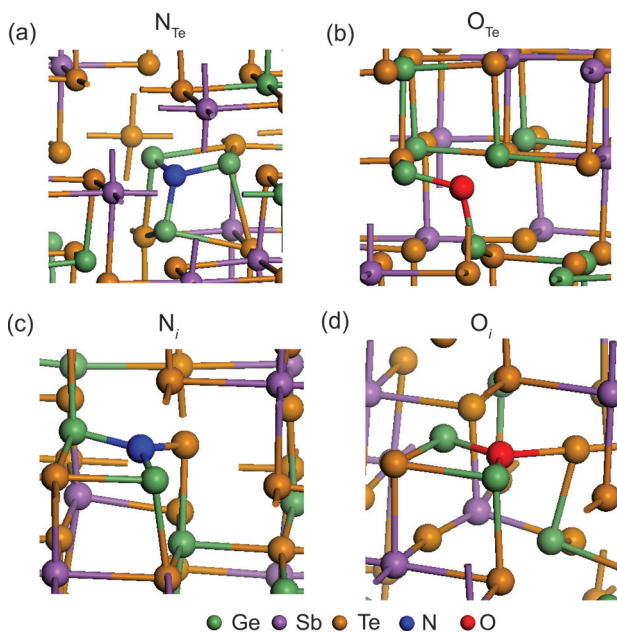


FIG. 2. (Color online) Representative local structures around dopants. (a) N_{Te} , (b) O_{Te} , (c) N_i , and (d) O_i .

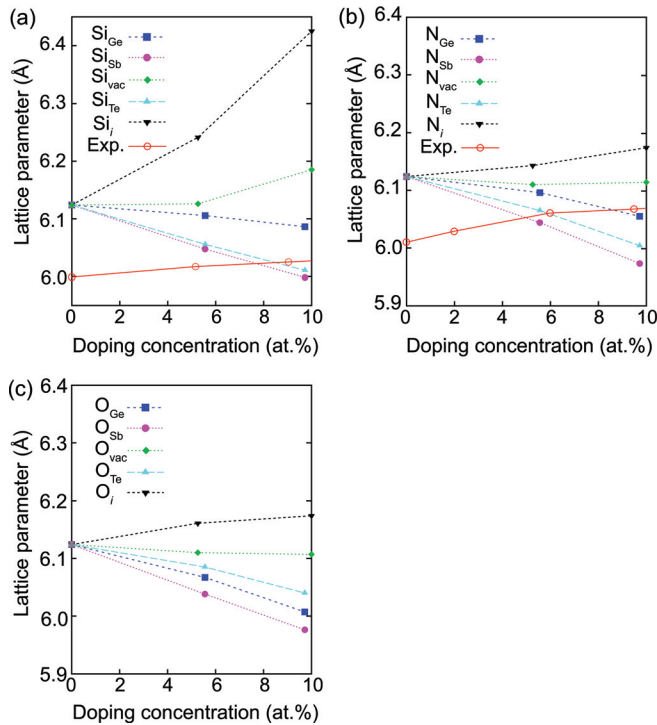


FIG. 3. (Color online) The lattice parameters of (a) Si-, (b) N-, and (c) O-doped crystalline $\text{Ge}_2\text{Sb}_2\text{Te}_5$ with respect to the doping concentration. In (a) and (b), experimental data are also provided.

N-doped c-GST are noted in Fig. 3(b) as empty circles.⁷ This experimental change is well explained by N_i dopants, supporting that significant amounts of N dopants exist in atomic states. (However, we also note that some experiment did not observe noticeable changes in the lattice parameter.⁴) Although there is no quantitative analysis, the x-ray diffraction data on O-doped c-GST in Ref. 14 are consistent with the increasing lattice parameters, which is also evidence of the interstitial form of O dopants because no other dopant types result in the volume expansion. The presence of dopants at interstitial sites, instead of substitutional ones, hints that dopants do not disturb the original stoichiometry of GST significantly.

C. Electronic structures of doped crystalline $\text{Ge}_2\text{Sb}_2\text{Te}_5$

To investigate how dopants affect electronic structures of c-GST, we calculate in Fig. 4 the density of states (DOS) for 72-atom supercells with 4 dopants at stable doping sites (~ 5 at. % doping concentrations). For the comparison purpose, DOS for undoped c-GST is also shown in Fig. 4(a). To analyze the electron localization, we calculate on the right scale the inverse participation ratio (IPR) defined as follows:

$$\text{IPR} = \frac{\sum_i |a_i|^4}{\left(\sum_i |a_i|^2\right)^2}, \quad (2)$$

where $|a_i|^2$ indicates the partial weight on the i th atom. IPR provides a convenient way to explore the spatial localization of a quantum state. For example, if the wave function is uniformly distributed over N atoms, IPR is equal to $1/N$.

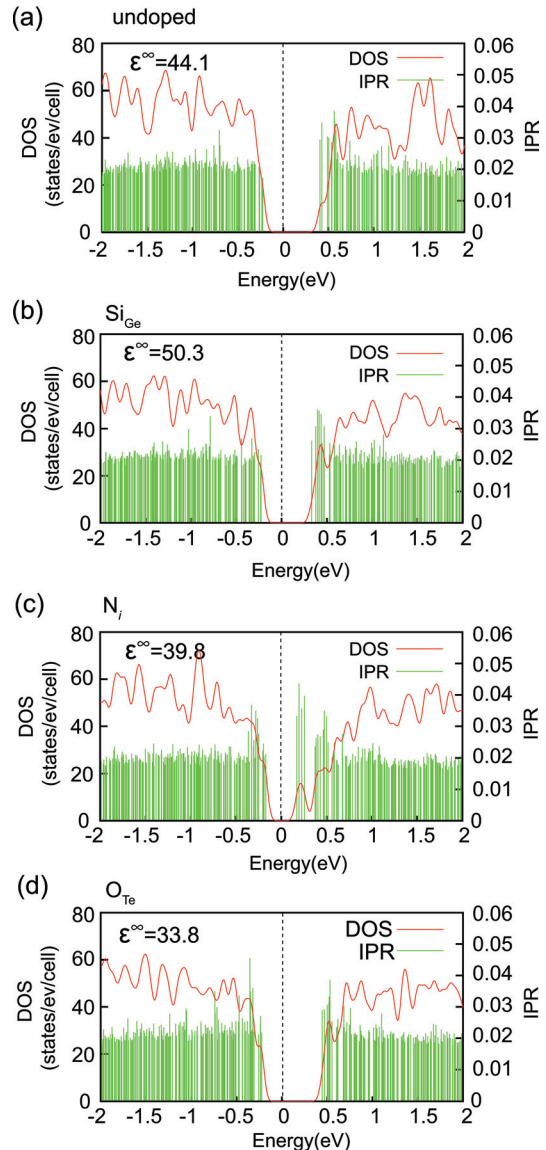


FIG. 4. (Color online) The density of states of c-GST with (a) no dopant, (b) Si_{Ge} , (c) N_i , and (d) O_{Te} . The inverse participation ratios (IPRs) are noted on the right scale. The computed optical dielectric constants with the diagonal average (ϵ^∞) are shown within each figure.

In Fig. 4, Si_{Ge} and N_i dopants reduce the energy gap while O_{Te} dopants increase the gap. To relate electronic structures to material properties, we calculate optical dielectric constants (ϵ^∞) using the linear response approach. The diagonally averaged ϵ^∞ is shown within each figure. The increase and decrease in ϵ^∞ for Si_{Ge} and O_{Te} , respectively, are consistent with the energy-gap variation because the smaller energy gap facilitates electronic polarization. However, the experiment in Ref. 14 showed that the refractive index (or ϵ^∞) of c-GST was increased with O dopants, which may imply that the change in macroscopic morphology such as the grain size would also affect the measured dielectric constant. In the case of N_i , ϵ^∞ is reduced in spite of the gap reduction. This is attributed to the enhanced electronic localization (see below) near valence and conduction edges compared to undoped c-GST since the localized state is less polarizable due to a large energy separation between bonding and antibonding states.

The increase of IPR near valence edges in N_i and O_{Te} means that electrons in this energy range are more localized than corresponding states in undoped c-GST. From the analysis on the spatial distribution of wave functions, these states are found to be distributed over dopant $2p$ and Te $5p$ orbitals. It is well established that c-GST behaves like a p -type semiconductor,³⁴ which is attributed to the formation of Ge vacancies.³⁵ Therefore, the localized states near the valence edges in N_i and O_{Te} imply that the dopants will play as strong scattering centers in p -type c-GST. This is consistent with experiment showing that the resistivity of c-GST increases with doping.^{2,9-11} By contrast, the influence of Si_{Ge} dopants on the conductivity of c-GST would be relatively weaker because IPR is very similar to that in undoped c-GST. In fact, it was observed in Ref. 3 that N-doped c-GST is more resistive than Si-doped samples with similar doping concentrations.

IV. DOPANTS IN AMORPHOUS $Ge_2Sb_2Te_5$

To obtain amorphous structures of doped GST, we carry out melt-quench MD simulations. The initial crystalline rock salt structures comprise 216 atoms and 12 dopants are introduced per unit supercell. Initially, Si dopants replace Ge atoms and N and O atoms are placed at interstitial positions. The resulting doping concentrations are 5.6 and 5.3 at. % for Si and N (or O) dopants, respectively. Since the accurate composition of doped GST is not available experimentally, the present choice of initial doping types should be regarded as one of the possibilities. To reflect the density reduction after amorphization, the supercell volume during melt-quench simulations is fixed to 7360 \AA^3 which is slightly larger than 6935 \AA^3 for undoped c-GST. As will be shown in the below, the final amorphous density varies depending on the dopant species. For melt-quench simulations, the temperature is increased to 2000 K and the system is melted for 12 ps to erase crystalline information. The liquid is then cooled to 1000 K and melted for 30 ps additionally. The liquid structure is subsequently quenched from 1000 to 300 K with a cooling rate of -15 K/ps . The final structure is fully relaxed at 0 K by optimizing lattice parameters and atomic positions.

A. Atomic structures of doped amorphous $Ge_2Sb_2Te_5$

The computed melt-quenched amorphous structures are shown in Figs. 5(a)–5(c). The main features can be summarized as follows.

1. Preferred bonding

In all cases, dopants bond with certain atomic species predominantly. Specifically, Si dopants mostly form bonds with Te atoms while Ge–N and Ge–O bonds prevail in N- and O-doped a-GST, respectively. This is quantitatively confirmed in Table I which shows coordination numbers (CNs) of dopant resolved with respect to atomic species. The cutoff radius (r_c) is set to the first dip position in the partial radial distribution function of each dopant. The average Ge–N and Ge–O separations are 1.98 and 1.94 \AA , respectively, which are similar to those in doped c-GST (see above).

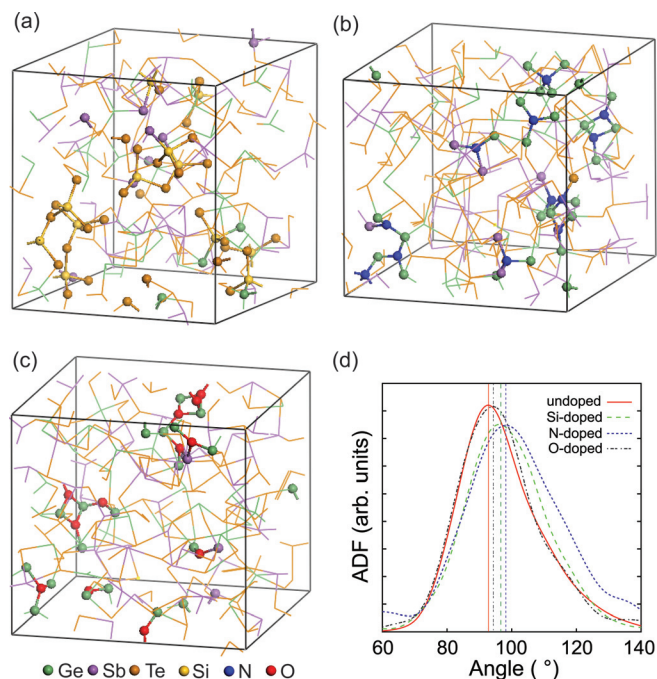


FIG. 5. (Color online) Amorphous structures of (a) Si-, (b) N-, and (c) O-doped GST. For the visual clarity, only dopants and their neighbors are drawn in ball-and-stick models. (d) The angle distribution functions (ADFs) around Ge atoms. The peak positions are noted as vertical lines.

2. Characteristic bonding geometry

It is seen in Fig. 5(a) that Si atoms bond with Te atoms with a tetrahedral geometry. This is in contrast to Ge atoms which exhibit both octahedral and tetrahedral configurations.²⁰ This is because the smaller atomic radius of Si favors sp^3 bonding over resonant-style p bonding. In Fig. 5(b), N dopants are mostly threefold coordinated with a planar bonding geometry. This is reminiscent of local structures in $\beta\text{-Ge}_3\text{N}_4$ (see Sec. III A). However, fourfold tetrahedral configurations are also identified with 4 out of 12 N dopants, which is confirmed by the average CN of 3.33 in Table I.

The bimodal CNs of N dopants can be rationalized by mixed nature of Ge configurations; in $\beta\text{-Ge}_3\text{N}_4$, all Ge atoms are tetrahedrally coordinated. However, in melt-quenched a-GST, both octahedral and tetrahedral configurations coexist.²⁰ The latter situation is rather close to spinel-type $\gamma\text{-Ge}_3\text{N}_4$ which is observed at high pressure conditions³⁶ and is less stable than $\beta\text{-Ge}_3\text{N}_4$ by 0.4 eV per formula unit within the present computational scheme. In $\gamma\text{-Ge}_3\text{N}_4$, two thirds of Ge atoms are sixfold coordinated and the remaining Ge atoms are fourfold coordinated. Interestingly, all N atoms in $\gamma\text{-Ge}_3\text{N}_4$ are fourfold coordinated with a configuration close to

TABLE I. Coordination numbers of dopants resolved with respect to neighboring species. The cutoff radii (r_c 's) were determined by the first-dip position in the partial radial distribution function around each dopant.

	r_c (\AA)	X-Ge	X-Sb	X-Te	Total
Si	2.9	0.42	0.67	2.92	4.00
N	2.4	2.75	0.50	0.08	3.33
O	2.3	2.25	0.33	0.00	2.58

the tetrahedral geometry. Therefore, the fourfold N atoms in a-GST can be regarded as a result of octahedral Ge atoms. The local configuration around O dopants in Fig. 5(c) can be understood in similar ways; in β -quartz GeO₂, all Ge atoms are in tetrahedral configurations and all O atoms are bivalent. By contrast, Ge atoms in rutile GeO₂ are close to octahedral coordination and O atoms are trivalent. We find that 7 out of 12 O dopants are trivalent, which is also consistent with the coexistence of two distinct types of Ge atoms.

3. Dopant clustering

In Figs. 5(a)–5(c), it is seen that dopants tend to cluster in small regions by often sharing Te or Ge atoms. As the initial distribution of dopants in c-GST was uniform and information of the initial structure was erased at 2000 K, the dopant clustering should be established during the melt-quench process. By closely monitoring atomic trajectories in MD simulations, we find that the dopants start to cluster around 700 K during the cooling process. The dopant clustering implies that repeated melt-quench cycles would eventually result in the phase separation of dopants into Ge₃N₄ or GeO₂, thereby degrading the device performance. It is interesting that neither N₂ molecules nor N–N bonds are identified in N-doped a-GST although forming N₂ molecule is energetically more favorable by 0.34 eV per N atom. (This is computed by $[E_{\text{tot}}(\text{N-doped a-GST}) - E_{\text{tot}}(\text{undoped a-GST}) + 6E_{\text{tot}}(\text{N}_2)]/12$.) This indicates that the energy barrier to form an N₂ molecule from atomically dissolved N atoms would be significant such that N₂ molecules are not easily generated during device operation.

4. Coordination numbers

The CNs for Ge, Sb, and Te atoms are shown in Table II. A cutoff radius of 3.2 Å is used when counting Ge, Sb, and Te neighbors but it is set to those of dopants in counting the bonds with dopants. In Si-doped a-GST, CNs are similar to those in undoped a-GST while the numbers of homopolar bonds such as Ge–Ge and Sb–Sb (given in parenthesis) are significantly reduced. In contrast, CNs are increased in N- and O-doped a-GST in comparison with undoped a-GST. In particular, the number of Te–Te pairs is noticeably increased, which is contrasted to the reduction of Ge–Te bonding fraction (not shown). This might be a consequence of abundant Ge–N and Ge–O bonds because these bonds deplete Ge neighbors around Te atoms. The reduction of Ge–Te bonds would weaken the covalent character of

Te-involved bonds and increase the metallic nature, which results in the increase of Te–Te bonds.

5. Angle distribution functions

It is known that the Ge atoms show the most dramatic change in the local order upon amorphization,²⁴ and therefore they are useful in inspecting the bonding nature of a-GST. In Fig. 5(d), the average angle distribution functions (ADFs) around Ge atoms are shown. The peak position for each a-GST is noted by a vertical line. Compared to undoped a-GST, the peak positions for Si- and N-doped a-GST shift to larger angles. In the case of N-doped a-GST, a shoulder develops around 109° which corresponds to the tetrahedral angle. This implies that N or Si dopants increase the portion of tetrahedral Ge atoms. For N-doped a-GST, this is because N atoms favor tetrahedral Ge atoms as shown in the most stable β -Ge₃N₄ phase. In Si-doped a-GST, the strong tendency of Si atoms to form *sp*³ bonds may have driven Ge atoms toward similar bonding configurations. In contrast, ADF of O-doped a-GST is similar to the undoped case. This is because O atoms equally favor tetrahedral and octahedral Ge atoms as inferred by the negligible energy difference between β -quartz and rutile phases of GeO₂ (see Sec. III A).

6. Ring structures and bond angles

An amorphous structure can be characterized by the statistics of ring structures which represent the irreducible closed bonding pathways. In particular, square motifs or fourfold rings similar to crystalline building blocks²¹ are found to be important in a-GST as it critically affects crystallization dynamics.²⁵ In Table II, the number of fourfold rings (N_{4r}) is presented for doped and undoped a-GST. The numbers in parentheses indicate fourfold rings that include at least one dopant. Due to the small atomic radii of N and O dopants, fourfold rings including these dopants significantly deviate from the square shape. It is found that N_{4r} is similar for all a-GST structures. This is a rather surprising result considering the significant influence of dopants on amorphous structures as revealed in the foregoing discussions. For example, the increase of tetrahedral Ge atoms indicates that the covalent nature of Ge atoms is enhanced. This would result in smaller N_{4r} as was demonstrated in the ideal glass structure which satisfies the 8–*N* rule and is most covalent among conceivable amorphous structures.²⁴ However, it was shown above that N dopants also increase CNs of Te atoms, away from two which is dictated by the 8–*N* rule. Therefore, the opposing effects of N dopants might be delicately

TABLE II. Structural properties of a-GST. The results for c-GST are also shown for comparison.

	Coordination numbers			Fourfold rings	Bond length (Å)	
	Ge (Ge-Ge)	Sb (Sb-Sb)	Te (Te-Te)		Ge-Te	Sb-Te
c-GST	6.00 (0.00)	6.00 (0.00)	4.80 (0.00)	106	2.90	3.05
a-GST	3.73 (0.29)	3.27 (0.50)	2.59 (0.23)	36	2.78	2.91
Si-doped a-GST	3.67 (0.11)	3.33 (0.29)	2.43 (0.22)	35 (3)	2.78	2.88
N-doped a-GST	4.00 (0.46)	3.46 (0.33)	2.64 (0.53)	40 (9)	2.78	2.92
O-doped a-GST	3.83 (0.17)	3.50 (0.25)	2.73 (0.45)	43 (3)	2.81	2.91

balanced and result in the similar N_{4r} to the undoped case. In Table II, we also examine average bond lengths in a-GST. It is found that Ge–Te and Sb–Te bond lengths change by less than 0.03 Å with doping. This is consistent with extended x-ray absorption fine structure (EXAFS) results in Ref. 12 which showed that N-doping up to 26 at. % did not affect Ge–Te distances. The small change also supports that the overall bonding character is not affected much by dopants.

7. Energetic stability

In Fig. 6(a), we plot the total energy difference per unit supercell between c-GST and a-GST [$\Delta E_{a-c} = E_{\text{tot}}(\text{a-GST}) - E_{\text{tot}}(\text{c-GST})$]. The total energies of initial crystalline structures confirm with formation energies in Fig. 1(b) for the same dopant type. ΔE_{a-c} for undoped GST is 78 meV/atom, which is similar to previous theoretical values^{21,24} but larger than the experimentally measured enthalpy difference marked as a filled triangle.⁷ For doped GST, ΔE_{a-c} is reduced substantially, and the values are in excellent agreements with experiment.^{7,14} However, considering the uncertainty in initial crystalline structures, the agreement with experiment should not be taken too literally. The reduction of ΔE_{a-c} is largely attributed to favorable dopant configurations in a-GST. That is to say, Si atoms in c-GST are enforced to make orthogonal bonding with neighbors while more favorable tetrahedral bonding geometry is formed in a-GST. On the other hand, N or O dopants in c-GST induce substantial lattice distortions in c-GST from large mismatch in atomic radii between dopants and host atoms. Such strain energies are partly relieved within the amorphous network. The smaller ΔE_{a-c} implies that the stability of a-GST is

increased with doping, which is consistent with the retarded crystallization found in all doped GST samples.

8. Atomic density

In Fig. 6(b), relaxed supercell volumes are compared between c-GST and a-GST (V_c and V_a , respectively). Interestingly, the dopant-dependent volume change is opposite between Si and O dopants. For example, Si dopants induce volume contraction in c-GST but volume expansion in a-GST. The reduction of CN of Si dopants from 6 to 4 should have contributed to increasing the specific volume of a-GST. The reverse relations are identified for O-doped GST as the dopant increases the amorphous density compared to the undoped a-GST. This implies that O dopants take up void spaces in a-GST and attract nearby Ge atoms. Similar effects might be present in N-doped GST as well but the density of N-doped a-GST is slightly smaller than for the undoped a-GST. This is likely to be caused by the increased tetrahedral Ge atoms whose CN is smaller than that of octahedral Ge atoms. The relative volume change, $(V_a - V_c)/V_c$, shown in the right scale is peaked at Si-doped GST and shows the minimum for O-doped GST. The smaller volume change in O-doped GST would reduce the residual stress within the PRAM cell during the phase transformation and increase the stability of a-GST.^{25,37}

B. Electronic structures of doped amorphous $\text{Ge}_2\text{Sb}_2\text{Te}_5$

In Figs. 7(b)–7(d), DOS and IPR for doped a-GST is shown. For comparison, the results for undoped a-GST are also presented in Fig. 7(a). In the case of N-doped GST, the localized peaks inside the energy gap of c-GST [see Fig. 4(c)] disappear in a-GST, which means that chemical bonding around N dopants is more stabilized in the amorphous structure. In Fig. 7, the energy gaps of all doped a-GST are increased compared to that for undoped a-GST. It is widely accepted that the carrier transport in a-GST is dominated by the Poole–Frenkel mechanism in which the charge carriers hop between trap centers via excitation above the mobility edges.³⁸ This indicates that the conductivity in a-GST is exponentially sensitive to the energy gap. Therefore, the increase of the energy gap for doped a-GST implies higher electrical resistivity, which is in line with experimental observations.^{9–11,39}

The computed ε^∞ for a-GST is shown within each figure. Regardless of dopants, ε^∞ of a-GST is significantly reduced from the crystalline value (~ 44). This is attributed to the loss of medium range order.²⁶ It is found that ε^∞ in Si-doped a-GST is reduced to 20.2 from 24.5 in the undoped a-GST, which is attributed to the gap increase. For N- and O-doped a-GST, energy gaps are also slightly increased but ε^∞ is almost unchanged from the value of the undoped case. IPR indicates that the states at conduction or valence edges are more delocalized than corresponding states in undoped a-GST. This may offset the effects of bandgap increase, resulting in similar ε^∞ . In some literatures,^{10,14} it was suggested that the dopants enhance the covalent nature in a-GST. If this is the case, the medium-range order would be disrupted

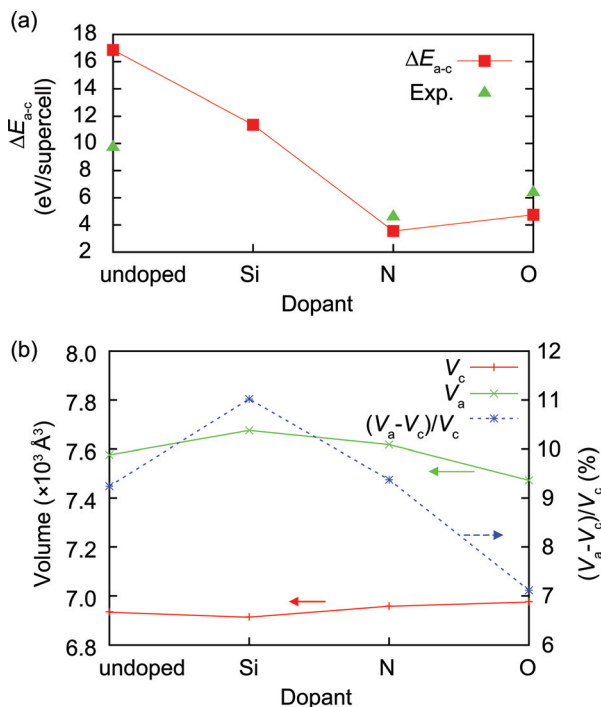


FIG. 6. (Color online) (a) Energy difference per supercell between a-GST and c-GST (ΔE_{a-c}). (b) The relaxed supercell volume for c-GST and a-GST with or without dopants. The relative volume expansion is shown on the right scale.

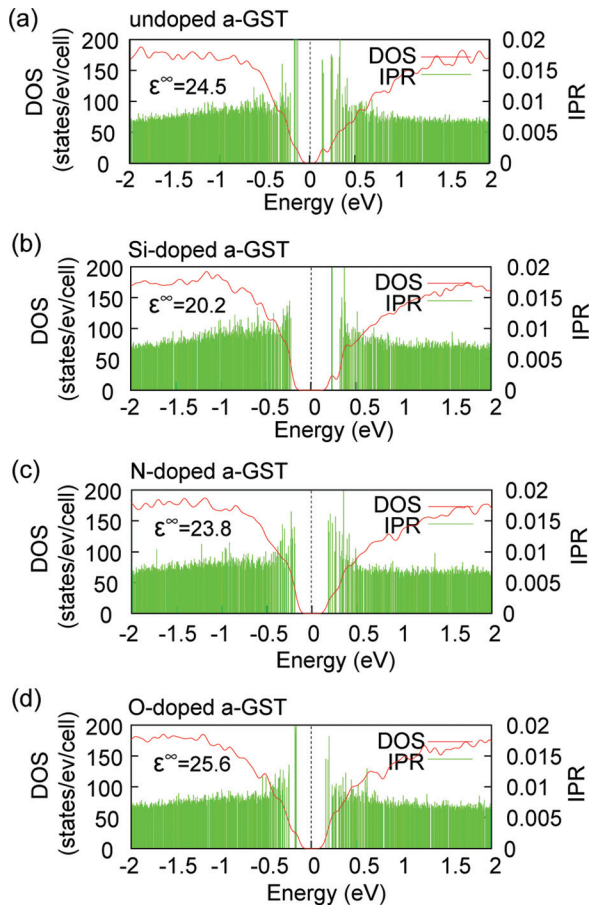


FIG. 7. (Color online) DOS and IPR for a-GST. The average optical dielectric constants are also shown within each figure.

because the covalent bonding tends to suppress resonant p bonding, resulting in smaller ϵ^∞ . However, this is not observed in the present study. Therefore, it is concluded that the overall bonding nature is not significantly affected by these dopants.

C. Crystallization of amorphous $\text{Ge}_2\text{Sb}_2\text{Te}_5$

In Sec. III, we investigated stable dopant positions by comparing total energies between probable sites in c-GST. In order to directly identify the dopant position in c-GST, we perform the annealing simulation on doped a-GST, with an expectation to recrystallize a-GST. This simulation is also useful in studying influence of dopants on crystallization dynamics. To reduce the computational cost, we employ 72-atom cell including one Si_{Ge} , N_i , and O_i dopant per unit cell. However, even with this relatively small supercell, the maximum simulation time that is feasible with the present computational resource is only ~ 1 ns which is one order shorter than the typical crystallization time of GST. In Ref. 25, we have shown that the compressive strain on a-GST accelerates the crystallization process. Employing this idea, we isotropically shrink the amorphous volume by 6% and anneal it at 650 K (just below melting points) up to 400 ps. This is followed by the -15 K/ps cooling to 300 K and full relaxation at 0 K. Figure 8(a) shows the total energy excluding the kinetic energy of ions. The energy zero is set to the total energy

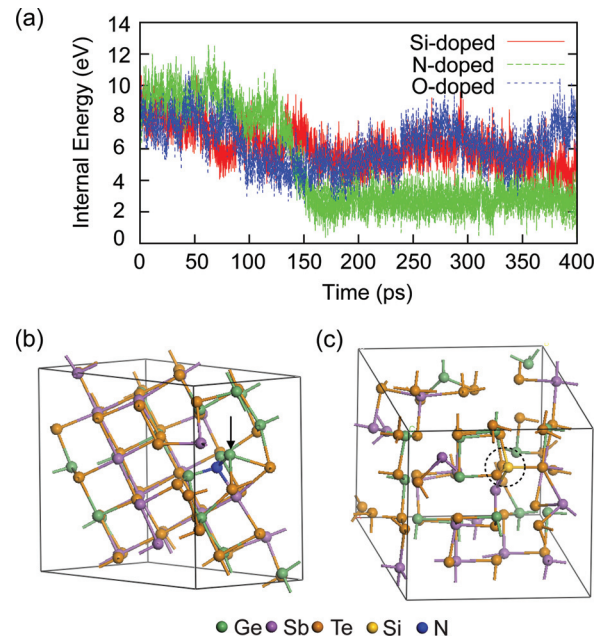


FIG. 8. (Color online) Crystallization dynamics of doped a-GST. (a) Temporal variation of internal energies of a-GST with respect to the annealing time. The annealing temperature is set to 650 K. (b) The final structure of N-doped GST obtained after annealing. A defective Ge atom is indicated by the arrow. (c) The final structure for Si-doped GST. The Si dopant is marked with a dashed circle.

of each doped a-GST at 0 K. While the internal energy of N-doped GST significantly drops at ~ 130 ps, those for Si- and O-doped a-GST do not change noticeably. The final relaxed structure for N-doped GST in Fig. 8(b) confirms that the crystallization is established. The energy difference between relaxed structures before and after annealing (ΔE_{anneal}) is -4.83 eV for N-doped GST. The magnitude of this value is significantly smaller than $\Delta E_{\text{a-c}}$ for undoped GST which is 6.87 eV for 72-atom cell, indicating that the relative stability of a-GST is enhanced with dopants. [Due to the size effect, this value is larger than one third of that for 216-atom cell in Fig. 6(a).] However, we note that the total energy of the final structure is higher by ~ 1.8 eV than 72-atom c-GST including one N_i dopant which was studied in Sec. III A. That is to say, the N-doped GST is crystallized into a metastable structure. This is attributed to structural defects induced by N dopants as will be discussed below. (For comparison, it was shown in Ref. 25 that the recrystallized undoped GST has an energy only ~ 0.1 eV higher than for the starting c-GST.) On the other hand, ΔE_{anneal} for Si-doped GST is -3.46 eV and the final structure in Fig. 8(c) indicates incomplete crystallization. Even though the variations of the internal energy of O-doped GST are similar to those of Si-doped GST, ΔE_{anneal} is only -1 eV for O-doped GST and the final structure is still close to the amorphous one. In Ref. 25, similarly pressurized a-GST underwent recrystallization at ~ 100 ps. The crystallization time of N-doped GST is slightly longer than this value. Therefore, it is apparent that N-doping with a concentration of 1.4 at. % is not enough to affect the crystallization dynamics of a-GST meaningfully. The retarded crystallization of N-doped GST might be a result of clustered dopants that exist at higher doping concentrations.

The N dopant in the crystallized GST is bonded with three Ge atoms and one Sb atom with mean distances of 2.02 and 2.39 Å, respectively [see Fig. 8(b)]. Among them, two of the three Ge atoms were bonded in the initial amorphous structure and they are not broken during the recrystallization process. The final structure in Fig. 8(b) is similar to N_{Te} or N_i studied in the above, which validates the energetic stability in Fig. 1(b) computed with crystalline structures. However, the Ge atom indicated by the arrow in Fig. 8(b) is not compatible with the rocksalt-style atomic registry and introduces significant lattice deformation around the dopant. To be specific, the defective Ge atom rotates the crystallographic orientations of neighboring Te atoms, which can be regarded as a primitive form of the grain boundary. On the other hand, neighboring atoms of Si (three Te atoms and one Sb atom) are different from the neighbors in the starting amorphous phase and they are bonded during annealing. This indicates that Si-Te bonds are weaker than Ge-N bonds. The Si dopant in Fig. 8(c) is still tetrahedrally coordinated even though most atoms are aligned with the rocksalt structure. This observation implies that the energy barrier from tetrahedral sp^3 bonding to orthogonal p -bonding network (so called “umbrella flipping”⁴⁰) would be significant for Si atoms, which would constitute a microscopic origin of the impeded crystallization in Si-doped GST.

V. CONCLUSIONS

In conclusion, we performed extensive *ab initio* calculations on the crystalline and amorphous structures of GST doped with Si, N, and O atoms, aiming to explain pronounced effects of dopants at the atomic level. In the crystalline phase, the most favorable doping site for Si was Si_{Ge} while N and O dopants favor interstitial or substitutional Te sites due to strong Ge-N or Ge-O bonds. However, the comparison of lattice parameters with experiment indicates that interstitial dopants should exist in significant amounts. The analysis on DOS indicates that the localization at the valence top increases for N- or O-doped c-GST, which increases resistivity of p -type c-GST. The amorphous structures of doped GST were obtained by melt-quench simulations. It was found that each dopant formed preferential bonding such as Si-Te, Ge-N, and Ge-O pairs. In particular, the local bonding structures around N or O atoms were well explained based on crystalline structures of Ge_3N_4 and GeO_2 . This is similar to the crystalline phase but the local bonding geometry is more favorable in the amorphous phase, which accounts for the increased stability of doped a-GST. The analysis on the local structure did not support the viewpoint that the bonding character is significantly changed toward the covalent character. The N dopant enhanced the covalent character of Ge but this was counterbalanced by the increased metallic nature of Te atoms. Nevertheless, Si atoms were found to be most effective in fundamentally affecting bonding nature of a-GST among the studied dopants. We also carried out annealing simulations on a-GST and the atomic structure of recrystallized N-doped GST was close to that for the N_i dopant in c-GST. However, the strong tendency of the N dopant to form bonds with Ge atoms gave

rise to significant lattice deformations akin to the grain boundary. The Si-doped GST was partially crystallized but Si atoms remained in the tetrahedral configuration. The comparison of the crystallization time with the undoped case directly confirmed that Si and O dopants slow down the crystallization process of a-GST. By enlightening the local structures of representative dopants and relating electronic and atomic structures to material properties, present theoretical results will serve as a useful guideline in choosing optimal dopants to engineer specific properties of GST.

ACKNOWLEDGMENTS

This work was supported by the National Program for 0.1 Terabit NVM Devices and the Fundamental R&D Program for Core Technology of Materials funded by the Ministry of Knowledge Economy of the Korean Government. Some parts of the computations were carried out at KISTI (KSC-2010-C2-0011).

- ¹A. L. Lacaita and D. J. Wouters, *Phys. Status Solidi A* **205**, 2281 (2008).
- ²B. Qiao, J. Feng, Y. Lai, Y. Ling, Y. Lin, T. Tang, B. Cai, and B. Chen, *Appl. Surf. Sci.* **252**, 8404 (2006).
- ³J. Feng, Y. Zhang, B. W. Qiao, Y. F. Lai, Y. Y. Lin, B. C. Cai, T. A. Tang, and B. Chen, *Appl. Phys. A* **87**, 57 (2007).
- ⁴H. Kölpin, D. Music, G. Lapyteva, R. Ghadimi, F. Merget, S. Richter, R. Mykhaylonka, J. Mayer, and J. M. Schneider, *J. Phys.: Condens. Matter* **21**, 435501 (2009).
- ⁵S. M. Kim, J. H. Jun, D. J. Choi, S. K. Hong, and Y. J. Park, *Jpn. J. Appl. Phys.* **44**, L208 (2005).
- ⁶R. Kojima, S. Okabayashi, T. Kashihara, K. Horai, T. Matsunaga, E. Ohno, N. Yamada, and T. Ohta, *Jpn. J. Appl. Phys., Part 1* **37**, 2098 (1998).
- ⁷T. H. Jeong, M. R. Kim, H. Seo, J. W. Park, and C. Yeon, *Jpn. J. Appl. Phys.* **39**, 2775 (2000).
- ⁸H. Seo, T.-H. Jeong, J.-W. Park, C. Yeon, S.-J. Kim, and S.-Y. Kim, *Jpn. J. Appl. Phys., Part 1* **39**, 745 (2000).
- ⁹H. Horii, J. H. Yi, J. H. Park, Y. H. Ha, I. G. Baek, S. O. Park, Y. N. Hwang, S. H. Lee, Y. T. Kim, K. H. Lee, U.-I. Chung, and J. T. Moon, in *Proceedings of the 2003 Symposium on VLSI Technology (IEEE, Piscataway, 2003)*, 177.
- ¹⁰S. Privitera, E. Rimini, and R. Zonca, *Appl. Phys. Lett.* **85**, 3044 (2004).
- ¹¹B. Liu, Z. Song, T. Zhang, J. Xia, S. Feng, and B. Chen, *Thin Solid Films* **478**, 49 (2005).
- ¹²Y. Kim, M. H. Jang, K. Jeong, M.-H. Cho, K. H. Do, D.-H. Ko, H. C. Sohn, and M. G. Kim, *Appl. Phys. Lett.* **92**, 061910 (2008).
- ¹³R. M. Shelby and S. Raoux, *J. Appl. Phys.* **105**, 104902 (2009).
- ¹⁴T. H. Jeong, H. Seo, K. L. Lee, S. M. Choi, S. J. Kim, and S. Y. Kim, *Jpn. J. Appl. Phys.* **40**, 1609 (2001).
- ¹⁵S. M. Jeong, K. H. Kim, S. M. Choi, and H. L. Lee, *Jpn. J. Appl. Phys.* **48**, 045503 (2009).
- ¹⁶K. B. Borisenko, Y. Chen, S. Song, and D. J. H. Cockayne, *Chem. Mater.* **21**, 5244 (2009).
- ¹⁷Z. Sun, J. Zhou, and R. Ahuja, *Phys. Rev. Lett.* **96**, 055507 (2006).
- ¹⁸J.-H. Eom, Y.-G. Yoon, C. Park, H. Lee, J. Im, D.-S. Suh, J.-S. Noh, Y. Khang, and J. Ihm, *Phys. Rev. B* **73**, 214202 (2006).
- ¹⁹J. Akola and R. O. Jones, *Phys. Rev. B* **76**, 235201 (2007).
- ²⁰S. Caravati, M. Bernasconi, T. D. Kühne, M. Krack, and M. Parrinello, *Appl. Phys. Lett.* **91**, 171906 (2007).
- ²¹J. Hegedus and S. R. Elliott, *Nat. Mater.* **7**, 399 (2008).
- ²²J. Akola, R. O. Jones, S. Kohara, S. Kimura, K. Kobayashi, M. Takata, T. Matsunaga, R. Kojima, and N. Yamada, *Phys. Rev. B* **80**, 020201(R) (2009).
- ²³Z. Sun, J. Zhou, A. Blomqvist, B. Johansson, and R. Ahuja, *Phys. Rev. Lett.* **102**, 075504 (2009).
- ²⁴E. Cho, J. Im, C. Park, W. J. Son, D. Kim, H. Horii, J. Ihm, and S. Han, *J. Phys.: Condens. Matter* **22**, 205504 (2010).
- ²⁵J. Im, E. Cho, D. Kim, H. Horii, J. Ihm, and S. Han, *Phys. Rev. B* **81**, 245211 (2010).
- ²⁶B. Huang and J. Robertson, *Phys. Rev. B* **81**, 081204(R) (2010).

- ²⁷Z. Sun, J. Zhou, H. Shin, A. Blomqvist, and R. Ahuja, *Appl. Phys. Lett.* **93**, 241908 (2008).
- ²⁸S. J. Kim, J. H. Choi, S. C. Lee, B. Cheong, D. S. Jeong, and C. Park, *J. Appl. Phys.* **107**, 103522 (2010).
- ²⁹G. Kresse and J. Hafner, *Phys. Rev. B* **47**, 558 (1993).
- ³⁰P. E. Blöchl, *Phys. Rev. B* **50**, 17953 (1994).
- ³¹J. P. Perdew, K. Burke, and M. Ernzerhof, *Phys. Rev. Lett.* **77**, 3865 (1996).
- ³²CRC Handbook of Chemistry and Physics, 66th ed., edited by R. C. Weast (CRC Press, Boca Raton, 1986).
- ³³K. Kim, J.-C. Park, J.-G. Chung, S. A. Song, M.-C. Jung, Y. M. Lee, H.-J. Shin, B. Kuh, Y. Ha, and J.-S. Noh, *Appl. Phys. Lett.* **89**, 243520 (2006).
- ³⁴B. S. Lee, J. R. Abelson, S. G. Bishop, D.-H. Kang, B. Cheong, and K.-B. Kim, *J. Appl. Phys.* **97**, 093509 (2005).
- ³⁵S. Caravati, M. Bernasconi, T. D. Kühne, M. Krack, and M. Parrinello, *J. Phys.: Condens. Matter* **21**, 255501 (2009).
- ³⁶J. Dong, O. F. Sankey, S. K. Deb, G. Wolf, and P. F. McMillan, *Phys. Rev. B* **61**, 11979 (2000).
- ³⁷M. Mitra, Y. Jung, D. S. Gianola, and R. Agarwal, *Appl. Phys. Lett.* **96**, 222111 (2010).
- ³⁸D. Ielmini and Y. Zhang, *J. Appl. Phys.* **102**, 054517 (2007).
- ³⁹Y. Kim, U. Hwang, Y. J. Cho, H. M. Park, M. -H. Cho, P. Cho, and J. Lee, *Appl. Phys. Lett.* **90**, 021908 (2007).
- ⁴⁰A. V. Kolobov, P. Fons, A. I. Frenkel, A. L. Ankudinov, J. Tominaga, and T. Uruga, *Nat. Mater.* **3**, 703 (2004).